A sensitive x-ray phase contrast technique for rapid imaging using a single phase grid analyzer

7 authors, including:

Kaye S Morgan
Monash University (Australia)
92 PUBLICATIONS   **732** CITATIONS

SEE PROFILE

Peter Modregger
University College London
64 PUBLICATIONS   **1,111** CITATIONS

SEE PROFILE

Vitaliy A. Guzenko
Paul Scherrer Institut
119 PUBLICATIONS   **1,760** CITATIONS

SEE PROFILE

Some of the authors of this publication are also working on these related projects:

Project Mixed beam radiotherapy View project

Project GOTTHARD View project

A sensitive x-ray phase contrast technique for rapid imaging using a single phase grid analyzer

Kaye S. Morgan,[1,*] Peter Modregger,[2,3] Sarah C. Irvine,[2,3] Simon Rutishauser,[2] Vitaliy A. Guzenko,[2] Marco Stampanoni,[2,4] and Christian David[2]

[1]*School of Physics, Monash University, Clayton, VIC 3800, Australia*

[2]*Paul Scherrer Institut, 5232 Villigen PSI, Switzerland*

[3]*École Polytechnique Fédérale de Lausanne, Lausanne 1015, Switzerland*

[4]*Institute for Biomedical Engineering, UZH/ETH Zürich, Zürich 8092, Switzerland*

Corresponding author: kaye.morgan@monash.edu

Phase contrast x-ray imaging (PCXI) is a promising imaging modality, capable of sensitively differentiating soft tissue structures at high spatial resolution. However, high sensitivity often comes at the cost of a long exposure time or multiple exposures per image, limiting the imaging speed and possibly increasing the radiation dose. Here, we demonstrate a PCXI method that uses a single short exposure to sensitively capture sample phase information, permitting high speed x-ray movies and live animal imaging. The method illuminates a checkerboard phase grid to produce a fine grid-like intensity reference pattern at the detector, then spatially maps sample-induced distortions of this pattern to recover differential phase images of the sample. The use of a phase grid is an improvement on our previous absorption grid work in two ways. There is minimal loss in x-ray flux, permitting faster imaging, and, a very fine pattern is produced for homogenous high spatial resolution. We describe how this pattern permits retrieval of five images from a single exposure; the sample phase gradient images in the horizontal and vertical directions, a projected phase depth image, an edge-enhanced image, and a type of scattering image. Finally, we describe how the reconstruction technique can achieve subpixel distortion retrieval and study the behavior of the technique in regard to analysis technique, Talbot distance, and exposure time.   © 2013 Optical Society of America

OCIS codes: (100.5070) Phase retrieval; (110.3010) Image reconstruction techniques; (170.3880) Medical and biological imaging; (340.6720) Synchrotron radiation; (340.7440) X-ray imaging; (350.2770) Gratings.

http://dx.doi.org/10.1364/OL.38.004605

Phase contrast x-ray imaging is already enabling new biomedical research, utilizing the x-ray phase properties of soft tissue to noninvasively capture biological structure and dynamics at high resolution. Analyzer-based phase contrast imaging [1] and Talbot grating interferometry [2–4] provide exquisite soft-tissue contrast and excel at structural characterization. The reduction in flux that comes with an analyzer crystal or the use of multiple exposures in Talbot grating interferometry can make high speed or live imaging difficult. Propagation-based phase contrast imaging [5,6] is often used for high speed imaging, but is less sensitive to gradual changes in sample thickness or composition, producing contrast primarily at edges.

Recent work has captured differential phase information with a single sample exposure through the use of a line [7,8] or mesh grid [9,10]. The grid is used to produce a reference intensity pattern, which is then distorted by the phase gradients in a sample (see Fig. 1). There are two different ways to analyze the resulting image and sensitively reveal phase gradients.

First, a Fourier method described by Takeda can be used [7,9,11]. In this approach, the Fourier transform of the image is taken and the peak corresponding to the grid frequency is centered and extracted (either by cropping or by filtering), then inverse-Fourier-transformed to produce a differential image. This method expects a grid image that is uniform in period across the image, particularly for quantitative retrieval. A calibration phantom can also be used for quantitative measurements [12].

Alternatively, the distortions in the grid can be mapped spatially by comparison with a reference image, using a local cross-correlation around each pixel to discover how far the pattern has shifted [10]. This method is more computationally expensive than the Fourier method, but the local pattern shifts can be easily converted to accurate quantitative measures of sample phase depth.

The spatial mapping approach does not require a single-frequency reference; hence both the reference object and reference-to-detector distance are far less constrained. For example, the absorption grid may be replaced by a piece of paper to create a random x-ray speckle pattern [13] at the sample [14,15]. This can be referred to "paper-analyzer" [14] or speckle-tracking [15] x-ray phase imaging. When specially manufactured gratings are not required, it is very easy to image a large field of view or to change the imaging energy or magnification. However, a random speckle pattern will likely have a range of feature sizes, slightly varying the achievable resolution across the image.

We address this through the use of a phase grating, which can be seen as either a uniform-feature-size "paper analyzer," a flux-efficient version of an absorption grating, or as a lens array in a Shack–Hartmann sensor [16].

When illuminated with x rays, a phase grid will produce a periodic intensity pattern with any propagation from the grid. This can be used in single-grid imaging, as shown in
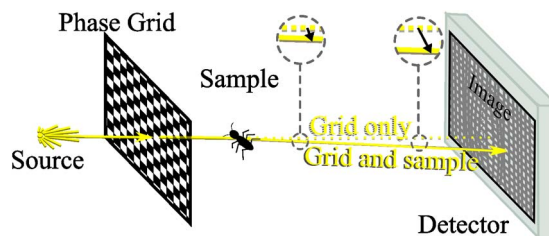

Fig. 1.   Experimental setup (not to scale).

Fig. 1, and with the spatial mapping method of analysis, the observed intensity does not need to be a single-frequency grid pattern. However, the analysis will work best for a high-visibility pattern, with visibility defined by Michelson [17]. As with Talbot interferometers, the maximum visibility pattern is observed at certain grid-to-detector distances depending on the grating parameters and x-ray energy. A checkerboard phase grating of period T illuminated by x rays of wavelength λ will produce a gridlike intensity pattern at distances D_n according to

$$D_n = nT^2/(8\lambda), \quad (1)$$

for $n = 1, 3, 5\ldots$ [18].

In this experiment, we used a checkerboard grating that produces 0 or π phase shifts when illuminated by 25 keV x rays, with a checkerboard period of 5.4 μm (15 pixels as imaged here). 25 keV is used for small animal imaging, a key application of this technique, balancing sufficient phase contrast with minimal absorption for fast imaging [19]. The checkerboard period was chosen to balance the ability of a fine grid to detect fine features in the sample with the need for a high-visibility reference pattern (visibility is affected by the detector point spread function, typically several pixels FWHM).

The grating pattern was produced by electron-beam writing into a resist layer and then transferred into the 300 μm thick silicon substrate by reactive ion etching [20]. For the setup described, grid-to-detector distance $D = 7.29$ cm, 21.87 cm, 36.45 cm, and so on.

An increase in the sample-to-detector distance will produce an increase in the transverse shift of the reference pattern, shown by the black arrow length in Fig. 1 insets. However, the shorter distances will produce the sharpest, most visible pattern (due to scattering and finite coherence length illumination). Short distances will also minimize the width and visibility of deleterious propagation-based phase contrast fringes seen from sharp edges in the sample [5,6]. These edge fringes can cause local errors in the tracking of the reference pattern [10]. To balance these effects, 21.87 cm was chosen in Fig. 2.

Experiments were conducted at the TOMCAT beamline at the Swiss Light Source (Figs. 2–4) and beamline BL20XU at SPring-8 (Figs. 5,6). At both, a lens-coupled scientific CMOS camera, the PCO.Edge, was used to capture images, with an effective pixel size of 0.36 μm.

The sample phase gradients were retrieved using the spatial mapping method described in Morgan *et al.* [10]. At each pixel in the image, this method takes a local cross-correlation between a small section of a "grid-only" image [Fig. 2(a)] and the corresponding section of a "sample-and-grid" image [Fig. 2(b)], to recover the transverse pattern shift (S) incurred by sample. The distance between the peak and the center will indicate the distance the reference pattern has locally shifted. Performing this mapping at each pixel in the image results in two differential contrast images, one showing the horizontal component of this shift [looks like Fig. 2(c)], and the other showing the vertical component [looks like Fig. 2(d)]. In this figure, the local sections were 8 pixels across and could move 4 pixels in each direction during the cross-correlation.
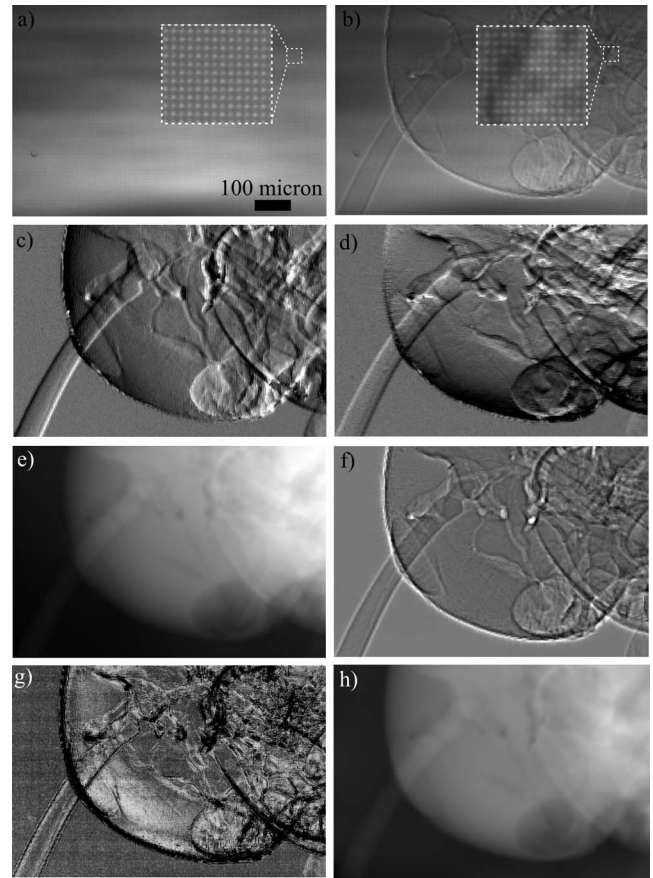

Fig. 2. Single-phase-grid PCXI images of an ant head, with 2.7 μm period grid pattern, 0.36 μm effective pixel size, 25 keV. The (a) grating-only image, (b) grating and sample image are all that is required to reconstruct (c) horizontal, (d) vertical phase gradients, (e) projected phase depth, (f) edge-enhanced attenuation image (like propagation-based PCXI), and (g) cross-correlation amplitude for scattering properties. For comparison to (e), (h) is the projected phase depth reconstructed from (f). In (a),(b), a larger Moiré grid may be seen depending on printer/viewer sampling.

In order to improve the performance at short propagation distances (chosen to minimize edge errors), an interpolation was introduced to locate the noninteger maximum of the cross-correlation. For each of the x and y direction, a quadratic is fitted to the three pixels at the maximum of the cross-correlation, and the peak of the quadratic taken as the true maximum. The fit and peak calculation can be easily performed in a single step,

$$S = (a_i - a_0) + (a_{i-1} - a_{i+1})/(2a_{i-1} - 4a_i + 2a_{i+1}), \quad (2)$$

where a is the cross-correlation array with maximum at position i, with the center of the cross-correlation at a_0.

The vertical and horizontal pattern shift images can be converted to images that describe the quantitative sample phase depth gradient (or thickness gradient for a single material sample), as per Morgan *et al.* [10]. These images [Figs. 2(c) and 2(d)] can be integrated together in Fourier space [21] to retrieve a projected thickness image [Fig. 2(e)]. If the sample extends beyond the field of view, as in Fig. 2, this reconstruction is much improved by tiling rotated and inverted versions of the gradient

images so as to form a complete sample surrounded by empty space, as per Bon *et al.* [22], before integrating.

Given that the local distortions in the reference pattern are known, the grid and sample image can be divided by a distorted grid-only image to effectively remove the grid image and recover a (degraded) propagation-based image of the sample [Fig. 2(f)]. The magnitude of the cross-correlation peak may also be plotted across the image, as seen in Fig. 2(g). If there are small sample features that scatter the x rays or that are comparable in size to the grid features, the visibility of the reference pattern will be decreased and hence the magnitude of the cross-correlation peak will decrease. This image is therefore an indicator of scattering or small structure properties of the sample. Figure 2(g) shows scattering from edges, but also distinctive areas on the side of the ant head that are not defined in the other images. Note that this image may need to be corrected using the grid-only image to isolate sample effects from uneven illumination or variations in the grid.

Finally [Fig. 2(h)], the phase reconstructed from the propagation-type image [Fig. 2(f)] [23], is visually inferior to the reconstruction from the single-grid images [Fig. 2(e)], since the shape of the ant head is better defined by the perpendicular gradient information than the edge information. For a quantitative comparison of recovered thickness by these two techniques, see [8,14].

This spatial mapping method of single-grid PCXI analysis is advantageous in two ways. First, it is insensitive to variations in the sample period across the image. The grid pattern need not be well aligned nor matched in size with the camera pixels. While the Fourier method of analysis can be performed on our images, as in Fig. 3, the variations in the observed grid pattern across the image are visible [Fig. 3(a)], and when corrected by comparison with the grid-only image, wrapping artifacts result, as seen on the antenna in Fig. 3(b). This phase wrapping can be corrected given a slowly varying sample, but makes automated analysis difficult.

Second, the spatial mapping method of analysis allows smaller features to be detected. The Fourier transform method results in an image with the resolution fundamentally reduced by a factor of $T/2b (= 7.5$ here), where T is the checkerboard grating period and b is the pixel size. While the spatial resolution of the image obtained using the spatial mapping method is not equal to the initial image resolution, smaller features are visible. In Fig. 4, there are 2–3 µm wide hairs on the ant head that can be detected using spatial mapping [Fig. 4(a); a bright, dark line], but cannot be accurately traced in the Fourier analysis images [Figs. 4(b), 4(c)].
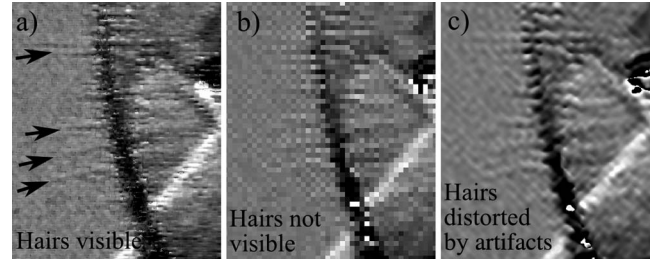
Fig. 4.   Magnification of Fig. 2(d), the phase gradient, by (a) the spatial mapping method; (b) by the Fourier method, cropping around the peak; and (c) by Fourier, bandpass filtering the peak (both with a window equal in width to the frequency of the grid).

Figure 4 also shows some background noise. Figure 5 shows that the spatial mapping technique performs slightly better than the Fourier method in regards to noise, for our dataset. While SNR will typically be linear with the square root of an exposure time, at very short exposure times the algorithms begin to break down. In the differential image retrieved by spatial mapping [Fig. 5(e)], "salt and pepper" noise appears where the correlation peak is not correctly located. However, this occurs at only 1.5% of the total pixels and can be removed to produce Fig. 5(f). The relative performance of the two analysis techniques will depend heavily on the periodicity and alignment of the grid pattern.

Figure 5 also demonstrates the ability of the method to detect both strong phase gradients (the sphere, which shows some edge errors) and very weak phase gradients (the polyethylene film, top right, with no edge errors).

The ability to accurately determine the pattern shift increases with both the visibility of the reference pattern
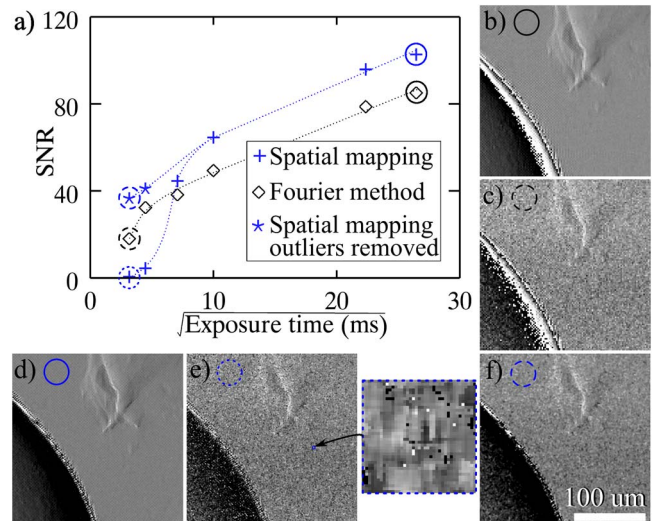
Fig. 5.   (a) Signal to noise ratio (SNR) in the flat area of the reconstructed differential phase image, shown as a function of exposure time. The images use (b) the Fourier method with 10 ms exposure (mean 700 raw counts) and (c) with 700 ms exposure (mean 47,000 raw counts), and use the spatial mapping method with (d) 700 ms exposure, (e) 10 ms exposure, and (f) 10 ms exposure with "salt and pepper" noise [inset of (e)] removed. The sample is a 1.5 mm diameter PMMA sphere and a 50 µm thin scrap of polyethylene (top of image), propagation 22 cm. To magnify noise detail, (b)–(f) show just 20% of the full field of view.
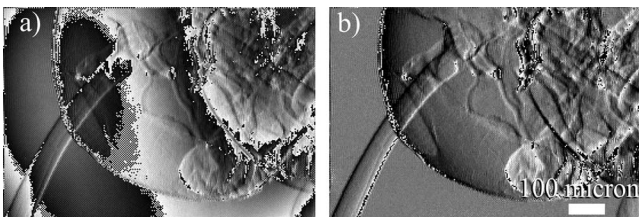

Fig. 3.   Fourier analysis [9,11] in Fig. 2(b) shows (a) horizontal gradients and (b) horizontal sample-only gradients, with non-sample gradients removed by subtracting the result of a Fourier analysis on the grid-only image [Fig. 2(a)] from Fig. 3(a).

and the sample-to-detector distance. However, these are linked, as the grid pattern visibility will decrease with increased grid-to-detector distance, as seen in Fig. 6(a) [24]. Measurements from a low-gradient region of the image [dotted line in Fig. 6(b)] shows that the low gradient SNR will initially increase with distance as the transverse shift in the reference pattern increases. However, at greater distances, the pattern visibility decreases and errors can result, particularly as the shift approaches the period of the grid pattern, as seen in Fig. 6(c) sphere.

As a rough rule, to prevent the grid pattern shifting over itself, the propagation distance Z, should obey

$$Z < T/2 \tan\left(\frac{1}{k}\frac{d\varphi}{dx}\right) \qquad (3)$$

for a maximum sample gradient of $d\phi/dx$, radiation of wavenumber $k = 2\pi/\lambda$ and checkerboard period T.

The balance between pattern visibility and transverse shift results in a maximum in the low gradient SNR at around 80 cm. With a significantly noisier raw image, the errors appear at shorter distances, as seen by the set of short exposure points, where the maximum low gradient SNR occurs close to 60 cm. If the region over which SNR is measured were to include the edge of the cylinder (i.e., a high phase gradient), the smaller distances, where edge errors are minimal, would perform much better [compare Fig. 6(b) to 6(c)]. The optimum distance is therefore defined for a given range of sample phase gradients (weaker samples require longer distances) and a given exposure time (shorter exposure times require shorter distances). A final factor to be considered is the effective source size, which can be reduced using apertures in order to increase the spatial coherence and hence the pattern visibility [with apertures that reduced the flux by 75% relative to Fig. 6(a), we measured visibility at 0.055 out to 80 cm].

In Fig. 6(c), the standard deviation in the flat part of the image is a shift of 0.018 μm, indicating an angular sensitivity of around 50 nrad. This is comparable to Talbot grating interferometry [24], indicating that spatial resolution is the main loss when using a single exposure.

We have shown a method of single phase-grid imaging with improved spatial resolution over our previous work,

and minimal loss in flux for increased speed in dynamic imaging applications. Five different high-speed movies [Figs. 2(c)–2(g)] can be created from a single raw sequence [Fig. 2(b)]. The best use of flux is also important in the transition of phase contrast techniques to the clinic, where radiation dose must be considered.

References

1. T. J. Davis, D. Gao, T. E. Gureyev, A. W. Stevenson, and S. W. Wilkins, Nature **373**, 595 (1995).
2. C. David, B. Nohammer, H. H. Solak, and E. Ziegler, Appl. Phys. Lett. **81**, 3287 (2002).
3. F. Pfeiffer, T. Weitkamp, O. Bunk, and C. David, Nat. Phys. **2**, 258 (2006).
4. A. Momose, W. Yashiro, Y. Takeda, Y. Suzuki, and T. Hattori, Jpn. J. Appl. Phys. **45**, 5254 (2006).
5. P. Cloetens, R. Barrett, J. Baruchel, J. P. Guigay, and M. Schlenker, J. Phys. D **29**, 133 (1996).
6. A. Snigirev, I. Snigireva, V. Kohn, S. Kuznetsov, and I. Schelokov, Rev. Sci. Instrum. **66**, 5486 (1995).
7. E. E. Bennet, R. Kopace, A. F. Stein, and H. Wen, Med. Phys. **37**, 6047 (2010).
8. K. S. Morgan, D. M. Paganin, and K. K. W. Siu, Opt. Lett. **36**, 55 (2011).
9. H. H. Wen, E. E. Bennett, R. Kopace, A. F. Stein, and V. Pai, Opt. Lett. **35**, 1932 (2010).
10. K. S. Morgan, D. M. Paganin, and K. K. W. Siu, Opt. Express **19**, 19781 (2011).
11. M. Takeda, H. Ina, and S. Kobayashi, J. Opt. Soc. Am. A **72**, 156 (1982).
12. J. Rizzi, P. Mercère, M. Idir, P. Da Silva, G. Vincent, and J. Primot, Opt. Express **21**, 17340 (2013).
13. M. J. Kitchen, D. Paganin, R. A. Lewis, N. Yagi, K. Uesugi, and S. T. Mudie, Phys. Med. Biol. **49**, 4335 (2004).
14. K. S. Morgan, D. M. Paganin, and K. K. W. Siu, Appl. Phys. Lett. **100**, 124102 (2012).
15. S. Bérujon, E. Ziegler, R. Cerbino, and L. Peverini, Phys. Rev. Lett. **108**, 158102 (2012).
16. S. C. Mayo and B. Sexton, Opt. Lett. **29**, 866 (2004).
17. A. A. Michelson, *Studies in Optics*, (University of Chicago, 1995).
18. I. Zanette, T. Weitkamp, T. Donath, S. Rutishauser, and C. David, Phys. Rev. Lett. **105**, 248102 (2010).
19. K. S. Morgan, M. Donnelley, D. M. Paganin, A. Fouras, N. Yagi, Y. Suzuki, A. Takeuchi, K. Uesugi, R. C. Boucher, D. W. Parsons, and K. K. W. Siu, PLOS ONE **8**, e55822 (2013).
20. S. Rutishauser, M. Bednarzik, I. Zanette, T. Weitkammp, M. Börner, J. Mohr, and C. David, Microelectron. Eng. **101**, 12 (2013).
21. C. Kottler, C. David, F. Pfeiffer, and O. Bunk, Opt. Express **15**, 1175 (2007).
22. P. Bon, S. Monneret, and B. Wattellier, Appl. Opt. **51**, 5698 (2012).
23. D. Paganin, S. C. Mayo, T. E. Gureyev, P. R. Miller, and S. W. Wilkins, J. Microsc. **206**, 33 (2002).
24. P. Modregger, B. R. Pinzer, T. Thüring, S. Rutishauser, C. David, and M. Stampanoni, Opt. Express **19**, 18324 (2011).
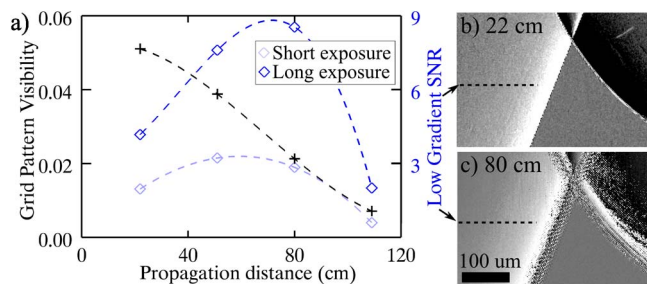
Fig. 6. (a) Grid pattern visibility as a function of grid-detector distance, and corresponding SNR along the profile shown in horizontal gradient images captured at (b) $D = 22$ cm and (c) $D = 80$ cm (long exp). This part of the image shows a 1.5 mm PMMA sphere (upper right corner of the image) and a 0.25 mm PMMA cylinder (left side of the image); short exposure = 30 ms, long = 600 ms. Points are fitted with a third-order spline to guide the eye.